Frontiers of Information Technology & Electronic Engineering
www.jzus.zju.edu.cn; engineering.cae.cn; www.springerlink.com
ISSN 2095-9184 (print); ISSN 2095-9230 (online)
E-mail: jzus@zju.edu.cn

Variational Bayesian multi-sparse component extraction for damage reconstruction of space debris hypervelocity impact*

Xuegang HUANG†‡, Anhua SHI, Qing LUO, Jinyang LUO

Hypervelocity Aerodynamics Institute, China Aerodynamics Research and Development Center, Mianyang 621000, China

†E-mail: emei-126@126.com

Received Oct. 25, 2020; Revision accepted Feb. 22, 2021; Crosschecked Feb. 14, 2022

Abstract: To improve the survivability of orbiting spacecraft against space debris impacts, we propose an impact damage assessment method. First, a multi-area damage mining model, which can describe damages in different spatial layers, is built based on an infrared thermal image sequence. Subsequently, to identify different impact damage types from infrared image data effectively, the variational Bayesian inference is used to solve for the parameters in the model. Then, an image-processing framework is proposed to eliminate variational Bayesian errors and compare locations of different damage types. It includes an image segmentation algorithm with an energy function and an image fusion method with sparse representation. In the experiment, the proposed method is used to evaluate the complex damages caused by the impact of the secondary debris cloud on the rear wall of the typical Whipple shield configuration. Experimental results show that it can effectively identify and evaluate the complex damage caused by hypervelocity impact, including surface and internal defects.

Key words: Hypervelocity impact; Variational Bayesian; Sparse representation; Damage assessment
https://doi.org/10.1631/FITEE.2000575 **CLC number:** TP301

1 Introduction

With the rapid development of aerospace science and technology and the strong desire of mankind to explore space, numerous spacecrafts have been launched into space. However, the large amount of space debris generated by space activities (Liou and Johnson, 2006) has a great impact on the on-orbit operations of spacecrafts (Huang et al., 2020). Due to the increasing frequency of impact events caused by small space debris, the damage assessment of spacecrafts is becoming progressively important. Infrared (IR) thermal imaging technology can achieve in-situ non-contact detection of defects by collecting and analyzing the small changes in the surface temperature fields of the test object under external thermal excitation. Because of its high efficiency, ease of visualization, and non-contact advantages, IR thermal imaging technology has begun to be applied in the field of aerospace damage detection and evaluation (Yin et al., 2019; Zhang et al., 2020). At the same time, various image sequence data processing methods have been developed to extract effective feature data related to defects from the original IR data. In Gao et al. (2016a), a linear model was used to describe the thermal images. Moreover, principal component analysis (PCA) (Geng et al., 2016) and independent component analysis (ICA) (Gao et al., 2016b) were used to highlight the damage-related information. In Sasmaz et al. (2015), Fourier

---

‡ Corresponding author

* Project supported by the National Natural Science Foundation of China (No. 61873305) and the Applied Basic Research Program of Sichuan Province, China (Nos. 2018JY0410 and 2019YJ0199)

ORCID: Xuegang HUANG, https://orcid.org/0000-0002-9168-3040

transform and other methods were used to reconstruct the defects in the images of the topography.

Since the data on the damaged area account for a small part of the overall test data, they can be realized as sparsity in the model. The sparsity model has been developed rapidly in many fields and is a powerful tool to solve the above problem. A sparsity model for solving multi-task problems in visual tracking scenarios has been established (Sun et al., 2019). Wang et al. (2018) proposed a joint model, which replaces the infinite space of pixels with a nonnegative space of pixels and is used to classify the hyperspectral images. To solve these models, many data-mining methods have been proposed. Peng et al. (2012) used robust PCA to decompose linear correlation images into low-rank and sparse matrices. Wu et al. (2018) established the multi-objective memetic method to obtain the sparse components of the considered image. The sparse nonnegative matrix factorization technique was applied by Guo and Zhang (2019). To meet the growing application requirements, numerous methods have been developed for sparse decomposition, such as cross-validation (CV) (Kokkinos and Margaritis, 2018), the Markov chain Monte Carlo (MCMC) method (Li et al., 2016), and the variational Bayesian (VB) method (Yang et al., 2018). These methods can be used to extract the damage-related information in the thermal image sequence.

In this study we develop an assessment method to achieve the hypervelocity impact damage assessment of spacecrafts. The main approach is summarized as follows: (1) A multi-area damage-mining model is proposed to effectively extract surface and subsurface damages by mining the thermal image sequence. (2) An overall damage assessment strategy is established by developing a framework for extraction of damage information by the VB method. (3) In the image fusion process based sparse representation (Ma et al., 2018; Kang et al., 2019), the IR image sequence is applied to the establishment of a dictionary since there are not enough historical data to construct its dictionary. Finally, the experimental results show the benefits of the developed method.

2 Proposed method

In the near-Earth space, there is a huge quantity of small space debris flying around the Earth at a super high speed. Since this tiny space debris cannot be tracked and cautioned against, the impact event caused by the tiny space debris is extremely harmful to orbiting spacecrafts. Due to the extremely high impact kinetic energy (I_{KE}) of space debris, its hypervelocity impact will cause not only visible damage on the surface such as surface impact craters and impact perforations, but also invisible subsurface damage such as back bulging and spalling. Taking the Whipple shield configuration commonly used in spacecrafts as an example, which consists of two layers of aluminum alloy thin plates with a certain distance between them, the secondary debris cloud generated by the impact of small space debris on the front bumper plate usually leads to a large-area impact crater on the rear wall and forms internal cracks and spalling damage on the subsurface of the rear wall (Fig. 1). The detection of damages caused by space debris impact requires simultaneous recognition of surface and subsurface damages, to provide comprehensive and accurate data for spacecraft risk assessment and on-orbit maintenance.

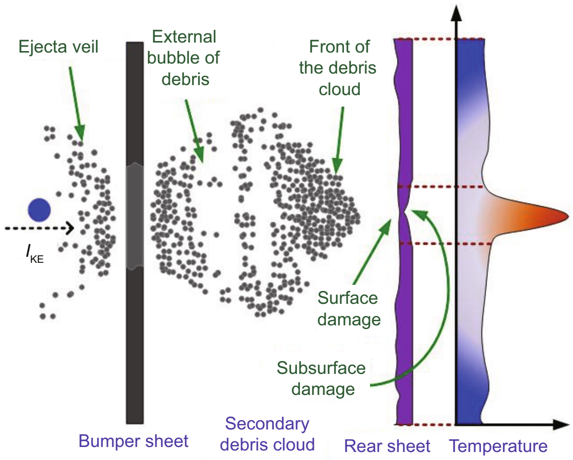

Fig. 1 Hypervelocity impact

2.1 Framework for damage assessment

In recent years, consequent to the rapid development of IR cameras, IR thermal imaging technology has provided a feasible way for the visual detection of defects and assessment of the surface damage in orbiting spacecrafts. IR imaging technology can unearth the difference in temperature field distribution among different damaged areas and normal areas based on temperature changes of the measured object. Hence, it is possible to extract and identify the characteristics of different types of damage by judging the differences in these transient thermal responses. How to develop an effective processing method to identify different types of damage is studied.

Since the IR thermal image sequence data contain the characteristic attributes of temperature in space and time, feature extraction is of utmost importance. Therefore, as shown in Fig. 2, we propose a detection framework to achieve the above purpose. In this framework, a multi-area damage-mining model is developed to obtain the images of damage from the thermal image sequence. Next, an image-processing method is built to reduce computational errors and data collection errors in the extraction process. In the detection framework, locations of different types of damage are also compared.

2.2 Multi-area damage-mining model

There exist certain requirements for how to evaluate the complex damage caused by impact on spacecraft surfaces, which means that the impact kinetic energy of space debris can be judged by comparing the degrees of damage by the same impact type. However, it is obvious that the damage caused by hypervelocity impact of space debris is usually more complex (Fig. 3). The damages at the same location may exist in different spatial layers. In this case, since the single IR image is only a two-dimensional (2D) image, the heat of the same pixel may be affected by multiple damages in different spatial layers. Hence, it is difficult to accurately evaluate the hypervelocity impact damage due to the differences in damage types. To distinguish the different damage types and accurately evaluate the degree of damage of materials subjected to hypervelocity impact, we propose a multi-area damage-mining model.

For convenience, a three-dimensional (3D) matrix block $\boldsymbol{\Xi} \in \mathbb{R}^{i \times j \times F_{\mathrm{t}}}$ is defined to denote the thermal image sequence, in which (i, j) and F_{t} denote the location coordinates and the time coordinate of the 3D matrix block, respectively. As shown in Fig. 4, the thermal image sequence contains different damage and non-damage information. Moreover, information on the different types of damage still shows mutual coupling. To eliminate this coupling and reconstruct the different types of damage from the IR thermal image sequence, the corresponding areas of the different damages will be described through their respective characteristic signals. Specifically, $\boldsymbol{X}_{\mathrm{F}}$ and $\boldsymbol{X}_{\mathrm{B}}$ express the surface damage and subsurface damage characteristics, respectively. Meanwhile, $\boldsymbol{X}_{\mathrm{N}}$ denotes the characteristics of the undamaged surface. Then, the multi-area damage-mining model is presented as follows:

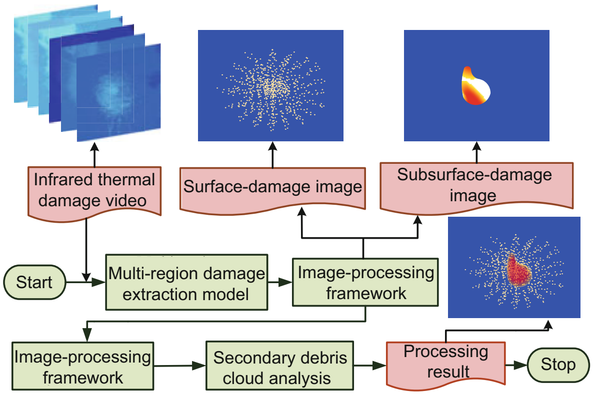

Fig. 2 Detection framework

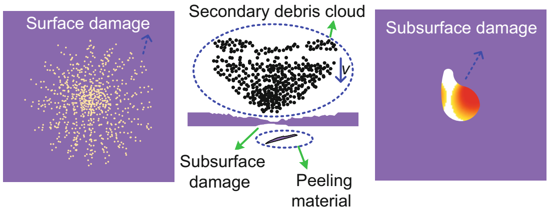

Fig. 3 Possible damage to the material

$$\boldsymbol{\Psi} = \overbrace{\sum_{t_{\mathrm{F}}=1}^{F_{t_{\mathrm{F}}}} \boldsymbol{X}_{\mathrm{F}}(t_{\mathrm{F}})\boldsymbol{\lambda}_{\mathrm{F}}(t_{\mathrm{F}})}^{\mathbf{Dam}_{\mathrm{F}}} + \overbrace{\sum_{t_{\mathrm{B}}=1}^{F_{t_{\mathrm{B}}}} \boldsymbol{X}_{\mathrm{B}}(t_{\mathrm{B}})\boldsymbol{\lambda}_{\mathrm{B}}(t_{\mathrm{B}})}^{\mathbf{Dam}_{\mathrm{B}}} + \overbrace{\sum_{t_{\mathrm{N}}=1}^{F_{t_{\mathrm{N}}}} \boldsymbol{X}_{\mathrm{N}}(t_{\mathrm{N}})\boldsymbol{\lambda}_{\mathrm{N}}(t_{\mathrm{N}})}^{\boldsymbol{B}} + \boldsymbol{N}, \tag{1}$$

where $\boldsymbol{\Psi} = [\mathrm{vec}(\boldsymbol{\Xi}(1)), \mathrm{vec}(\boldsymbol{\Xi}(2)), \ldots, \mathrm{vec}(\boldsymbol{\Xi}(F_{\mathrm{t}}))] \in \mathbb{R}^{K \times F_{\mathrm{t}}}$ is converted from $\boldsymbol{\Xi}$ with $K = i \times j$ ("vec" is an operator converting a block into a vector), $\boldsymbol{X}_{\mathrm{F}} \in \mathbb{R}^{K \times F_{t_{\mathrm{F}}}}$, $\boldsymbol{X}_{\mathrm{B}} \in \mathbb{R}^{K \times F_{t_{\mathrm{B}}}}$, $\boldsymbol{X}_{\mathrm{N}} \in \mathbb{R}^{K \times F_{t_{\mathrm{N}}}}$. $\boldsymbol{X}_{\mathrm{B}}(t_{\mathrm{B}})$, $\boldsymbol{X}_{\mathrm{F}}(t_{\mathrm{F}})$, and $\boldsymbol{X}_{\mathrm{N}}(t_{\mathrm{N}})$ are the column vectors of $\boldsymbol{X}_{\mathrm{B}}$, $\boldsymbol{X}_{\mathrm{F}}$, and $\boldsymbol{X}_{\mathrm{N}}$, respectively. Their respective mixing parameter matrices can be expressed as $\boldsymbol{\lambda}_{\mathrm{F}} \in \mathbb{R}^{F_{t_{\mathrm{F}}} \times F_{\mathrm{t}}}$, $\boldsymbol{\lambda}_{\mathrm{B}} \in \mathbb{R}^{F_{t_{\mathrm{B}}} \times F_{\mathrm{t}}}$, and $\boldsymbol{\lambda}_{\mathrm{N}} \in \mathbb{R}^{F_{t_{\mathrm{N}}} \times F_{\mathrm{t}}}$. $\boldsymbol{\lambda}_{\mathrm{F}}(t_{\mathrm{F}})$, $\boldsymbol{\lambda}_{\mathrm{B}}(t_{\mathrm{B}})$, and $\boldsymbol{\lambda}_{\mathrm{N}}(t_{\mathrm{N}})$ are the row vectors of $\boldsymbol{\lambda}_{\mathrm{F}}$, $\boldsymbol{\lambda}_{\mathrm{B}}$, and $\boldsymbol{\lambda}_{\mathrm{N}}$, respectively. $\boldsymbol{N}$ denotes the noise matrix.

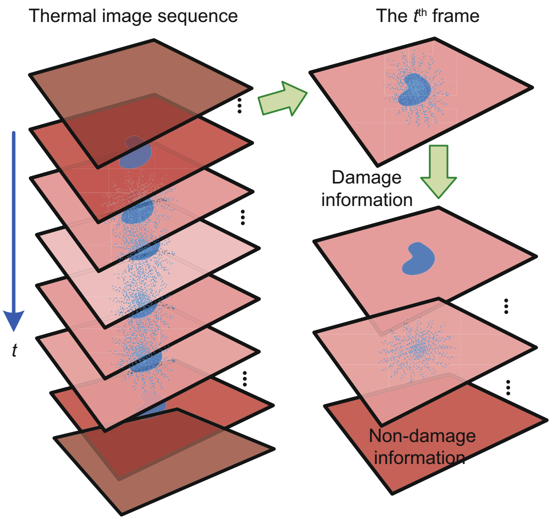

Fig. 4 Possible damages in different layers

The linear combination of characteristics of the normal area without damage can be obtained by a low-rank matrix $\boldsymbol{B}=\left(\boldsymbol{U}\boldsymbol{\Sigma}^{1/2}\right)\left(\boldsymbol{V}\boldsymbol{\Sigma}^{1/2}\right)^{\mathrm{T}}=\boldsymbol{S}\boldsymbol{T}^{\mathrm{T}}$, in which $\boldsymbol{S}\in\mathbb{R}^{K\times r}$, $\boldsymbol{T}\in\mathbb{R}^{F_{\mathrm{t}}\times r}$ (r is the dimension of $\boldsymbol{\Sigma}$). Each column of this matrix is designed to obey the Gaussian distribution with precision of ϱ_i and mean of zero. Furthermore, ϱ_i obeys the Gamma distribution $p(\varrho_i)=\Gamma(u,\frac{1}{v})\propto\varrho_i^{u-1}\exp(-v\varrho_i)$, where u and v are hyperparameters. Moreover, surface and subsurface damages are expressed separately as the sparse matrices $\mathbf{Dam}_{\mathrm{F}}$ and $\mathbf{Dam}_{\mathrm{B}}$. Each element also obeys the Gaussian distribution with precision of ϖ_{ij} and υ_{ij}, and mean of zero. Moreover, ϖ_{ij} and υ_{ij} separately represent information affecting the surface and subsurface damage temperature distributions. They are determined by the characteristics of different types of damage and obey Jeffreys priors, i.e., $p(\varpi_{ij})=(\varpi_{ij})^{-1}$, $p(\upsilon_{ij})=(\upsilon_{ij})^{-1}$. Assume that the noise is Gaussian white noise, i.e., $p(\boldsymbol{N}|\boldsymbol{\iota})=N(\boldsymbol{N}|\boldsymbol{0},\boldsymbol{\iota}^{-1}\boldsymbol{I}_{KF_{\mathrm{t}}})$, in which $p(\boldsymbol{\iota})=\boldsymbol{\iota}^{-1}$ and $\boldsymbol{I}_{KF_{\mathrm{t}}}$ denotes a KF_{t}-dimensional unit matrix. Thus, the posterior probability of the thermal image sequence can be derived using the following expression:

$$\begin{aligned}&p(\boldsymbol{\Psi}|\boldsymbol{S},\boldsymbol{T},\mathbf{Dam}_{\mathrm{F}},\mathbf{Dam}_{\mathrm{B}},\boldsymbol{\iota})\\=&\prod_i\prod_j N(\boldsymbol{\Psi}|\boldsymbol{S}\boldsymbol{T}^{\mathrm{T}}+\mathbf{Dam}_{\mathrm{F}}+\mathbf{Dam}_{\mathrm{B}},\boldsymbol{\iota}^{-1}\boldsymbol{I}_{KF_{\mathrm{t}}}).\end{aligned}\tag{2}$$

The joint probability of the multi-area damage-mining model can be represented as follows:

$$\begin{aligned}&p(\boldsymbol{\Psi},\boldsymbol{S},\boldsymbol{T},\mathbf{Dam}_{\mathrm{F}},\mathbf{Dam}_{\mathrm{B}},\boldsymbol{\varrho},\boldsymbol{\varpi},\boldsymbol{\upsilon},\boldsymbol{\iota})\\=&p(\boldsymbol{\Psi}|\boldsymbol{S},\boldsymbol{T},\mathbf{Dam}_{\mathrm{F}},\mathbf{Dam}_{\mathrm{B}},\boldsymbol{\iota})p(\boldsymbol{S}|\boldsymbol{\varrho})p(\boldsymbol{T}|\boldsymbol{\varrho})\\&\cdot p(\mathbf{Dam}_{\mathrm{F}}|\boldsymbol{\varpi})p(\mathbf{Dam}_{\mathrm{B}}|\boldsymbol{\upsilon})p(\boldsymbol{\varrho})p(\boldsymbol{\varpi})p(\boldsymbol{\upsilon})p(\boldsymbol{\iota}).\end{aligned}\tag{3}$$

To mine the damage features of different areas, VB uses the mean field theory (MFT) to estimate the parameters. Each hidden variable's posterior probability can be obtained by minimizing the Kullback–Leibler (KL) divergence (Kullback and Leibler, 1951). Furthermore, $\boldsymbol{Z}=(\boldsymbol{S},\boldsymbol{T},\mathbf{Dam}_{\mathrm{F}},\mathbf{Dam}_{\mathrm{B}},\boldsymbol{\varrho},\boldsymbol{\varpi},\boldsymbol{\upsilon},\boldsymbol{\iota})$ is used to represent the set of hidden variables. Then, the estimation of the posterior probability of the hidden variable $Q(\boldsymbol{Z}_k)$, where $k=1,2,\ldots,8$, can be written as

$$\ln(Q(\boldsymbol{Z}_k))=\langle\ln(p(\boldsymbol{\Psi},\boldsymbol{Z}))\rangle_{\boldsymbol{Z}\neq\boldsymbol{Z}_k}+\chi,\tag{4}$$

in which $\langle\cdot\rangle$ denotes the expectation and χ is a constant.

1. Estimation of $\boldsymbol{S}$ and $\boldsymbol{T}$

Each row of $\boldsymbol{S}$ obeys the Gaussian distribution. Their respective probabilities are expressed as $Q\left(\boldsymbol{s}_{i\star}\right)=N(\boldsymbol{s}_{i\star}|\left\langle\boldsymbol{s}_{i\star}\right\rangle,\boldsymbol{\Sigma}^S)$, $Q\left(\boldsymbol{t}_{j\star}\right)=N(\boldsymbol{t}_{j\star}|\left\langle\boldsymbol{t}_{j\star}\right\rangle,\boldsymbol{\Sigma}^T)$, and their respective means are written as

$$\langle\boldsymbol{s}_{i\star}\rangle^{\mathrm{T}}=\langle\boldsymbol{\iota}\rangle\boldsymbol{\Sigma}^S\langle\boldsymbol{T}\rangle^{\mathrm{T}}(\boldsymbol{\psi}_{i\star}-\mathbf{Dam}_{\mathrm{F}_{i\star}}-\mathbf{Dam}_{\mathrm{B}_{i\star}})^{\mathrm{T}},\tag{5}$$

$$\langle\boldsymbol{t}_{j\star}\rangle^{\mathrm{T}}=\langle\boldsymbol{\iota}\rangle\boldsymbol{\Sigma}^T\langle\boldsymbol{S}\rangle^{\mathrm{T}}(\boldsymbol{\psi}_{\star j}-\mathbf{Dam}_{\mathrm{F}_{\star j}}-\mathbf{Dam}_{\mathrm{B}_{\star j}})^{\mathrm{T}},\tag{6}$$

where $\boldsymbol{s}_{i\star}$ and $\boldsymbol{t}_{j\star}$ denote the rows of $\boldsymbol{S}$ and $\boldsymbol{T}$, respectively. Moreover, $\boldsymbol{\psi}_{i\star}$ ($\boldsymbol{\psi}_{\star j}$), $\mathbf{Dam}_{\mathrm{F}_{i\star}}$ ($\mathbf{Dam}_{\mathrm{F}_{\star j}}$), and $\mathbf{Dam}_{\mathrm{B}_{i\star}}$ ($\mathbf{Dam}_{\mathrm{B}_{\star j}}$) represent the rows (columns) of $\boldsymbol{\Psi}$, $\mathbf{Dam}_{\mathrm{F}}$, and $\mathbf{Dam}_{\mathrm{B}}$, respectively. $\boldsymbol{\Sigma}^S=(\langle\boldsymbol{\iota}\rangle\left\langle\boldsymbol{T}^{\mathrm{T}}\boldsymbol{T}\right\rangle+\boldsymbol{\gamma})^{-1}$ and $\boldsymbol{\Sigma}^T=(\langle\boldsymbol{\iota}\rangle\left\langle\boldsymbol{S}^{\mathrm{T}}\boldsymbol{S}\right\rangle+\boldsymbol{\gamma})^{-1}$ represent the variances of $\boldsymbol{S}$ and $\boldsymbol{T}$ respectively, in which the diagonal matrix $\boldsymbol{\gamma}=\mathrm{diag}(\varrho_1,\varrho_2,\ldots,\varrho_r)$ and $\boldsymbol{B}=\langle\boldsymbol{S}\rangle\langle\boldsymbol{T}\rangle^{\mathrm{T}}$.

2. Estimation of $\boldsymbol{\varrho}$

The ϱ_j distribution and its mean can be written as

$$\langle\varrho_j\rangle=\frac{K+F_{\mathrm{t}}+2u}{\left\langle\boldsymbol{s}_{\star j}^{\mathrm{T}}\boldsymbol{s}_{\star j}\right\rangle+\left\langle\boldsymbol{t}_{\star j}^{\mathrm{T}}\boldsymbol{t}_{\star j}\right\rangle+2v},\tag{7}$$

where $\boldsymbol{s}_{\star j}$ and $\boldsymbol{t}_{\star j}$ denote the columns of $\boldsymbol{S}$ and $\boldsymbol{T}$, respectively. $\left\langle\boldsymbol{s}_{\star j}^{\mathrm{T}}\boldsymbol{s}_{\star j}\right\rangle=\left\langle\boldsymbol{s}_{\star j}\right\rangle^{\mathrm{T}}\left\langle\boldsymbol{s}_{\star j}\right\rangle+K(\Sigma^S)_{jj}$ and $\left\langle\boldsymbol{t}_{\star j}^{\mathrm{T}}\boldsymbol{t}_{\star j}\right\rangle=\left\langle\boldsymbol{t}_{\star j}\right\rangle^{\mathrm{T}}\left\langle\boldsymbol{t}_{\star j}\right\rangle+F_{\mathrm{t}}(\Sigma^T)_{jj}$, in which $(\Sigma^S)_{jj}$

and $(\Sigma^T)_{jj}$ denote the $(j,j)^{\mathrm{th}}$ entry of $\boldsymbol{\Sigma}^S$ and $\boldsymbol{\Sigma}^T$, respectively.

3. Estimation of $\mathbf{Dam}_{\mathrm{F}}$ and $\mathbf{Dam}_{\mathrm{B}}$

$\mathrm{Dam}_{\mathrm{F}_{ij}}$ and $\mathrm{Dam}_{\mathrm{B}_{ij}}$ obey the Gaussian distribution. Their probabilities are respectively written as follows:

$$Q(\mathrm{Dam}_{\mathrm{F}_{ij}}) = N\left(\mathrm{Dam}_{\mathrm{F}_{ij}} \middle| \left\langle \mathrm{Dam}_{\mathrm{F}_{ij}} \right\rangle, \Sigma_{ij}^{\mathrm{Dam}_{\mathrm{F}}}\right),$$
$$Q(\mathrm{Dam}_{\mathrm{B}_{ij}}) = N\left(\mathrm{Dam}_{\mathrm{B}_{ij}} \middle| \left\langle \mathrm{Dam}_{\mathrm{B}_{ij}} \right\rangle, \Sigma_{ij}^{\mathrm{Dam}_{\mathrm{B}}}\right).$$

Their means are respectively written as follows:

$$\left\langle \mathrm{Dam}_{\mathrm{F}_{ij}} \right\rangle = \frac{\langle \boldsymbol{\iota} \rangle \left(\psi_{ij} - \langle \boldsymbol{s}_{i\star} \rangle \langle \boldsymbol{t}_{j\star} \rangle^{\mathrm{T}} - \left\langle \mathrm{Dam}_{\mathrm{B}_{ij}} \right\rangle\right)}{\langle \boldsymbol{\iota} \rangle + \langle \varpi_{ij} \rangle}, \tag{8}$$

$$\left\langle \mathrm{Dam}_{\mathrm{B}_{ij}} \right\rangle = \frac{\langle \boldsymbol{\iota} \rangle \left(\psi_{ij} - \langle \boldsymbol{s}_{i\star} \rangle \langle \boldsymbol{t}_{j\star} \rangle^{\mathrm{T}} - \left\langle \mathrm{Dam}_{\mathrm{F}_{ij}} \right\rangle\right)}{\langle \boldsymbol{\iota} \rangle + \langle \upsilon_{ij} \rangle}, \tag{9}$$

where $\Sigma_{ij}^{\mathrm{Dam}_{\mathrm{F}}} = (\langle \boldsymbol{\iota} \rangle + \langle \varpi_{ij} \rangle)^{-1}$ and $\Sigma_{ij}^{\mathrm{Dam}_{\mathrm{B}}} = (\langle \boldsymbol{\iota} \rangle + \langle \upsilon_{ij} \rangle)^{-1}$ represent the variances of $\mathbf{Dam}_{\mathrm{F}}$ and $\mathbf{Dam}_{\mathrm{B}}$, respectively.

4. Estimation of $\boldsymbol{\varpi}$, $\boldsymbol{\upsilon}$, and $\boldsymbol{\iota}$

The posterior probabilities of ϖ_{ij}, υ_{ij}, and $\boldsymbol{\iota}$ obey the Gamma distribution. Their means are respectively represented as follows:

$$\langle \varpi_{ij} \rangle = \frac{1}{\left\langle \mathrm{Dam}_{\mathrm{F}_{ij}}^2 \right\rangle} = \frac{1}{\left\langle \mathrm{Dam}_{\mathrm{F}_{ij}} \right\rangle^2 + \Sigma_{ij}^{\mathrm{Dam}_{\mathrm{F}}}}, \tag{10}$$

$$\langle \upsilon_{ij} \rangle = \frac{1}{\left\langle \mathrm{Dam}_{\mathrm{B}_{ij}}^2 \right\rangle} = \frac{1}{\left\langle \mathrm{Dam}_{\mathrm{B}_{ij}} \right\rangle^2 + \Sigma_{ij}^{\mathrm{Dam}_{\mathrm{B}}}}, \tag{11}$$

$$\langle \boldsymbol{\iota} \rangle = \frac{K F_{\mathrm{t}}}{\left\langle \left\| \boldsymbol{\Psi} - \boldsymbol{S}\boldsymbol{T}^{\mathrm{T}} - \mathbf{Dam}_{\mathrm{F}} - \mathbf{Dam}_{\mathrm{B}} \right\|_{\mathrm{F}}^2 \right\rangle}, \tag{12}$$

in which $\left\langle \left\| \boldsymbol{\Psi} - \boldsymbol{S}\boldsymbol{T}^{\mathrm{T}} - \mathbf{Dam}_{\mathrm{F}} - \mathbf{Dam}_{\mathrm{B}} \right\|_{\mathrm{F}}^2 \right\rangle = \left\| \boldsymbol{\Psi} - \langle \boldsymbol{S} \rangle \langle \boldsymbol{T} \rangle^{\mathrm{T}} - \langle \mathbf{Dam}_{\mathrm{F}} \rangle - \langle \mathbf{Dam}_{\mathrm{B}} \rangle \right\|_{\mathrm{F}}^2 + \mathrm{tr}(F_{\mathrm{t}} \langle \boldsymbol{S} \rangle^{\mathrm{T}} \langle \boldsymbol{S} \rangle \boldsymbol{\Sigma}^T) + \mathrm{tr}(K \langle \boldsymbol{T} \rangle^{\mathrm{T}} \langle \boldsymbol{T} \rangle \boldsymbol{\Sigma}^S) + \mathrm{tr}(K F_{\mathrm{t}} \boldsymbol{\Sigma}^S \boldsymbol{\Sigma}^T) + \sum_{i=1}^{K} \sum_{j=1}^{F_{\mathrm{t}}} \Sigma_{ij}^{\mathrm{Dam}_{\mathrm{F}}} + \sum_{i=1}^{K} \sum_{j=1}^{F_{\mathrm{t}}} \Sigma_{ij}^{\mathrm{Dam}_{\mathrm{B}}}$. Here, $\mathrm{tr}(\cdot)$ denotes the trace of the corresponding matrix. Finally, the matrix of the model can be derived by optimizing the parameters under the above iteration (Eqs. (5)–(12)). Each column of $\mathbf{Dam}_{\mathrm{F}}$ and $\mathbf{Dam}_{\mathrm{B}}$ can be represented as the corresponding images $\boldsymbol{S}_{\mathrm{F}}$ and $\boldsymbol{S}_{\mathrm{B}}$ respectively, which can highlight the damaged and undamaged regions and describe the features of real damage.

The characteristic images of the different damaged regions can be obtained by solving the multi-region damage-mining model. Furthermore, to more accurately evaluate the degree of damage by the hypervelocity impact, further processing of the above-mentioned images with the damage characteristics is required.

Remark 1 VB is a class of techniques used in Bayesian estimation and machine learning to approximate intractable integrals. It is used mainly in complex statistical models, generally including three types of variables, i.e., observed variables (data), unknown parameters (parameters), and latent variables. It has two main purposes: one is to approximate the posterior probability of unobservable variables so that statistical inferences can be made from these variables; the other is to give a lower bound of the marginal likelihood function of the observed variables for a particular model. It is believed that the higher the edge likelihood value of the model, the better the model fits these variables and the higher the probability that the model generates data. In this study, a multi-area damage-mining model, which can describe damages in different spatial layers, is built based on the IR thermal image sequence. To identify different types of impact damage from IR image data effectively, VB is used to solve for the parameters in the model.

2.3 Image-processing framework

2.3.1 Noise elimination

By taking the pixels in the same damaged area as a whole and fully considering all the damages to evaluate the damage to the material, an image-processing framework is proposed in this subsection to process the damage-related images. The temperature difference among adjacent pixels in the same damage area is small, and the degree of this temperature difference can be measured by variance. To simultaneously analyze the temperature distribution of the pixel points in the same damaged area, the different areas of the same image are divided by curve C. Meanwhile, the energy distribution is established by the temperature variance $\left|T - \bar{T}\right|^2$ (T represents the temperature and $\bar{T}$ represents the average temperature). It should be mentioned that the higher the energy, the greater the temperature difference. The following expression of the energy function is built based on the total energy of the damaged and undamaged regions:

$$\begin{aligned}&\varXi(T_1,T_2,\vartheta)\\=&\alpha_1\int\limits_{\varTheta}\left|S_{\mathrm{B}}(x,y)-T_1\right|^2 H_\varepsilon(\vartheta(x,y,t))\mathrm{d}x\mathrm{d}y\\&+\alpha_2\int\limits_{\varTheta}\left|S_{\mathrm{B}}(x,y)-T_2\right|^2(1-H_\varepsilon(\vartheta(x,y,t)))\mathrm{d}x\mathrm{d}y,\end{aligned}\tag{13}$$

where $\boldsymbol{S}_{\mathrm{B}}$ denotes the damage image and $\vartheta(x,y,t)$ represents the dividing curve C at time t, i.e., $\vartheta(x,y,t)=0$. Clearly, $\vartheta(x,y,t)>0$ when pixel (x,y) is inside C; otherwise, define $\vartheta(x,y,t)<0$ when (x,y) is outside C. $H_\varepsilon(\vartheta)=\frac{1}{2}(1+\frac{2}{\pi}\arctan(\frac{\vartheta}{\varepsilon}))$ is the Heaviside function. Furthermore, α_1 and α_2 denote weights, and T_1 and T_2 represent the average temperatures inside and outside C respectively:

$$\begin{aligned}T_1&=\frac{\int_{\varTheta}S_{\mathrm{B}}(x,y)H_\varepsilon(\vartheta(x,y,t))\mathrm{d}x\mathrm{d}y}{\int_{\varTheta}H_\varepsilon(\vartheta(x,y,t))\mathrm{d}x\mathrm{d}y},\\T_2&=\frac{\int_{\varTheta}S_{\mathrm{B}}(x,y)(1-H_\varepsilon(\vartheta(x,y,t)))\mathrm{d}x\mathrm{d}y}{\int_{\varTheta}(1-H_\varepsilon(\vartheta(x,y,t)))\mathrm{d}x\mathrm{d}y}.\end{aligned}$$

The first term of $\varXi(T_1,T_2,\vartheta)$ represents the variance of the temperature in the inner area of C. Its second term denotes the variance of the temperature value in the area outside C. When the energy function reaches a minimum, the temperatures of the pixels in the inner area of the dividing curve are similar; accordingly, these pixels should belong to the same area. Similarly, the external pixels belong to the same area. By minimizing $\varXi(T_1,T_2,\vartheta)$ and searching the optimal curve, the image is divided into the damaged region and the undamaged region. Then, the pixel points in the same area are regarded as a whole, so that more accurate damage images can be obtained according to the temperature distribution.

To obtain the minimum value of $\varXi(T_1,T_2,\vartheta)$, the Euler–Lagrange equation (Yang et al., 2018; Zong et al., 2019) is used to solve the energy function. The variation of the dividing curve is $\frac{\partial\vartheta}{\partial t}=\delta_\varepsilon(\vartheta)[-\alpha_1(S_{\mathrm{B}}(x,y)-T_1)^2+\alpha_2(S_{\mathrm{B}}(x,y)-T_2)^2]$, where $\delta_\varepsilon(\vartheta)=\frac{1}{\pi}\frac{\varepsilon}{\varepsilon^2+\vartheta^2}$. We solve the final dividing curve $\vartheta^*(x,y,t)$ by iterating T_1, T_2, and $\frac{\partial\vartheta}{\partial t}$. Subsequently, the temperature distribution of the image is set to $\boldsymbol{S}_{\mathrm{B}}^*=\boldsymbol{S}_{\mathrm{B}_{\max}}*H_\varepsilon(\vartheta^*)$, where $\boldsymbol{S}_{\mathrm{B}_{\max}}$ represents the maximum temperature of the original image.

By establishing $\varXi(T_1,T_2,\vartheta)$, more accurate images of the different types of damage can be derived. The different damage types are integrated by image fusion to investigate the interaction between them. Image fusion technology merges the information of two or more images into one image, so that the fused image contains more information, which is more convenient for human analysis or computer processing. Therefore, the sparse representation method is used in the following fusion process.

2.3.2 Image fusion

1. Establishment of the dictionary

In the usual sparse representation method, a large number of data samples can be used to construct a complete dictionary. However, due to the high cost of hypervelocity impact testing, it is difficult to obtain a large number of test data samples. To solve the above problem, we build an overcomplete dictionary based on the IR thermal image sequence. It should be noted that the temperature of the material changes gradually during the heating process, so the temperature distribution between adjacent frames is similar. To reduce the calculation time and improve processing efficiency, frames with similar temperature distributions can be merged through preprocessing before the establishment of the dictionary. The developed algorithm is presented as follows:

Step 1: Set $\varrho=1$. The thermal image sequence is merged to valid frames by K-means clustering. Each frame is split to blocks with size $n\times n$. Meanwhile, each block is converted into a vector by the "vec" operator. Moreover, it is normalized to composite the sample set $\boldsymbol{Z}\in\mathbb{R}^{M_{\mathrm{Z}}\times F_{\mathrm{Z}}}$, where $M_{\mathrm{Z}}=n\times n$ and $F_{\mathrm{Z}}=\frac{F_x}{n}\times\frac{F_y}{n}\times K$. The dictionary $\boldsymbol{D}\in\mathbb{R}^{M_{\mathrm{D}}\times F_{\mathrm{D}}}$ is initialized randomly, where $M_{\mathrm{D}}=n\times n$ and F_{D} represents the amount of data in the dictionary. We define a zero matrix as the initial sparse matrix $\boldsymbol{H}\in\mathbb{R}^{F_{\mathrm{D}}\times F_{\mathrm{Z}}}$ and initialize the maximum number of iterations G.

Step 2: Initialize residual $\mathbf{e}^\omega=\boldsymbol{Z}_{\star i}$ $(i=1,2,\ldots,F_{\mathrm{Z}})$, the sparse degree τ, and the allowable error ε. Let $\omega=1$.

Step 3: Find the best matching atom $\mathbf{Dam}_{\star j*^\omega}$ by matching separately index set $I^\omega=I^{\omega-1}\cup j*^\omega$ and atom set $\phi^\omega=\phi^{\omega-1}\cup\mathbf{Dam}_{\star j}$ based on $j*^\omega=\underset{j\in[1,F_{\mathrm{D}}]}{\arg\max}\,|\langle\mathbf{e}^\omega,\mathbf{Dam}_{\star j}\rangle|$. Let $\omega=\omega+1$. Solve

$\boldsymbol{H}_i^{\omega} = \arg\min\limits_{\boldsymbol{H}_i} \|\boldsymbol{Z}_{\star i} - \phi^{\omega}\boldsymbol{H}_i\|_2^2$ and update the sparse coefficient according to $\boldsymbol{H}_i^{\omega}$.

Step 4: Calculate $\mathbf{e}^{\omega} = \boldsymbol{Z}_{\star i} - \phi^{\omega-1}\boldsymbol{H}_i$. If $\|\mathbf{e}^{\omega}\| < \varepsilon$ or $\omega > \tau$, then $\boldsymbol{H}_{\star i}$ is used to express the sparse coefficient of $\boldsymbol{Z}_{\star i}$; otherwise, go to step 3. Calculate the sparse coefficients of all F_{Z} blocks. A sparse matrix $\boldsymbol{H}$ is applied to denote them.

Step 5: Let ${}_{\mathrm{temp}}\boldsymbol{D} = \boldsymbol{D}$ and ${}_{\mathrm{temp}}\boldsymbol{H} = \boldsymbol{H}$. Find the sparse coefficient ${}_{\mathrm{temp}}\boldsymbol{H}_{i'\star}$ (the $(i')^{\mathrm{th}}$ row of $\boldsymbol{H}$) of the $(i')^{\mathrm{th}}$ atom in the dictionary ${}_{\mathrm{temp}}\mathbf{Dam}_{\star i'}, i' = 1, 2, \ldots, F_{\mathrm{D}}$. Find the non-zero term in ${}_{\mathrm{temp}}\boldsymbol{H}_{i'\star}$ to form ${}_{\mathrm{temp}}\boldsymbol{H}_{i'I}^{\text{non-zero}}$, where $I = \{\imath | \boldsymbol{H}_{i'\imath} \neq \mathbf{0}, \imath = 1, 2, \ldots, F_{\mathrm{Z}}\}$.

Step 6: Find blocks $\boldsymbol{Z}_{\star I}$ corresponding to I in $\boldsymbol{Z}$, to form the matrix ${}_{\mathrm{temp}}\boldsymbol{Z}$, and perform singular value decomposition on ${}_{\mathrm{temp}}\boldsymbol{Z}$ (${}_{\mathrm{temp}}\boldsymbol{Z} = \boldsymbol{U\Sigma V}^{\mathrm{T}}$). Then, update the atom $\mathbf{Dam}_{\star i'} = \boldsymbol{U}_{\star 1}$ and sparse coefficient ${}_{\mathrm{temp}}\boldsymbol{H}_{i'\star}$ based on $\boldsymbol{H}_{i'I} = \Sigma_{11}\boldsymbol{V}_{\star 1}^{\mathrm{T}}$. Update all atoms in the dictionary.

Step 7: Let $\varrho = \varrho + 1$, and go back to step 2 until $\varrho > G$. Finally, one can obtain the dictionary $\boldsymbol{D}$ and sparse coefficient $\boldsymbol{H}$.

2. Image fusion

After the dictionary is built, the images of the different damage types are sparsely represented by the orthogonal matching pursuit (OMP) algorithm (Chen et al., 2019) based on the dictionary, and the sparse coefficients are then fused as follows: $\boldsymbol{H}_{\mathrm{fusion}} = \max\{\boldsymbol{H}_{\mathrm{F}}, \boldsymbol{H}_{\mathrm{B}}\}$, where $\boldsymbol{H}_{\mathrm{F}}$ and $\boldsymbol{H}_{\mathrm{B}}$ represent the sparse coefficients of the images of the different layers. Then, the fused sparse coefficient and dictionary ($\boldsymbol{S} = \boldsymbol{D}\boldsymbol{H}_{\mathrm{fusion}}$) can be applied to derive the fused image. Fig. 5 shows the process of image fusion with sparse representation.

Since the thermal image sequence contains abundant information on the characteristics of the material's damages, it can be used to construct a dictionary. In addition, the sparse representation represents a large number of images by sparse signals, so the required storage space is greatly reduced. The application of image fusion technology can effectively synthesize the characteristic information and location information of different damage defects, thereby improving the utilization of image information and accuracy of computer interpretation.

3 Experimental results

To obtain the samples of hypervelocity impact damage for IR thermal imaging detection, we used two typical Whipple shield configurations as test pieces. The hypervelocity impact tests of space debris were carried out on the hypervelocity ballistic equipment in the China Aerodynamics Research and Development Center (CARDC), as shown in Fig. 6. The aluminum projectile with a diameter of about 5 mm was accelerated to about 8 km/s by the two-stage light gas gun, which collided vertically with the Whipple shield configurations. The bumper plate was penetrated by the hypervelocity aluminum projectile, producing the secondary debris cloud. The damage status of the rear walls caused by the impact of the debris cloud is shown in Figs. 7 and 8. There are a lot of tiny impact craters on the front

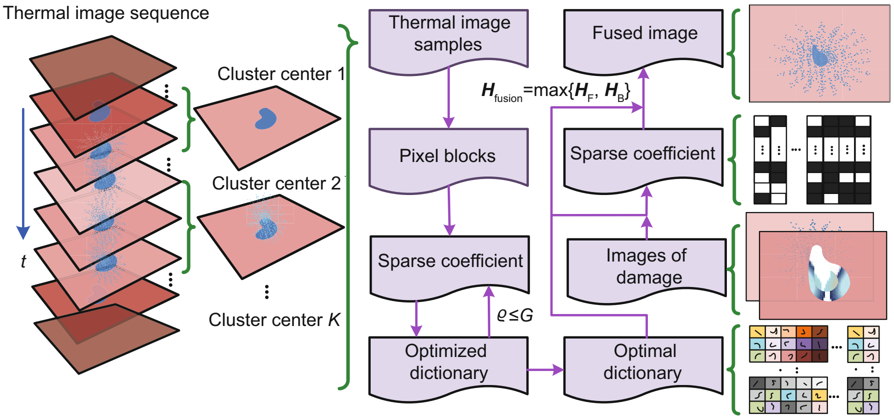

Fig. 5 Image fusion based on sparse representation

surface of the rear wall. Although no perforations were found, spalling damage was formed on the subsurface or back of the rear wall. In the next step, the hypervelocity impact damage samples were thermally excited by two halogen lamps, and the surface temperature distribution of the test piece was recorded by the IR camera (Fig. 9). The resolution of the IR image was 512 × 640, and the number of acquisition frames was 362.

To carry out data processing, the 3D thermal image sequences were transformed into a 2D matrix. The matrix was further processed through PCA, such that frames with 95% important information were derived to replace all the images in the sequence. Then, VB was used to solve the model, in which the iteration number was set as 100. Parameters u and v were set to 10^{-6}. Finally, the images of surface damage and subsurface damage caused by two impacts at different speeds can be denoted by the columns of matrices $\mathbf{Dam}_{\mathrm{F}}$ and $\mathbf{Dam}_{\mathrm{B}}$, respectively. Images with the strongest contrast in the different damaged regions were chosen. For material I, the experimental results are displayed in Fig. 10.

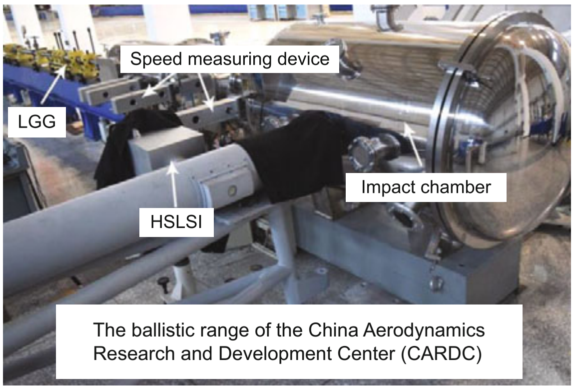

Fig. 6 Setup for the hypervelocity impact experiment


(a) (b)

Fig. 7 Test piece I: (a) surface; (b) subsurface


(a) (b)

Fig. 8 Test piece II: (a) surface; (b) subsurface

Figs. 10a and 10b show the surface and subsurface damage images of material I, respectively. From the subsurface damage image, it is seen that some noise may be caused by the data acquisition and independence assumption of pixels. Hence, an energy function was used to judge the damage region by considering the heat distribution of the pixels in the area comprehensively. In the process of optimizing the energy function, the iteration number was set as 20 and the initial segmentation curve was selected artificially. The value of the pixel was set to $\boldsymbol{S}_{\mathrm{B}}^{*} = \boldsymbol{S}_{\mathrm{B}_{\max}} * H_{\varepsilon}(\vartheta^{*})$. Finally, the result of the subsurface damage images is shown in Fig. 11, in which the red area represents the region of damage.

By comparison with the subsurface damage

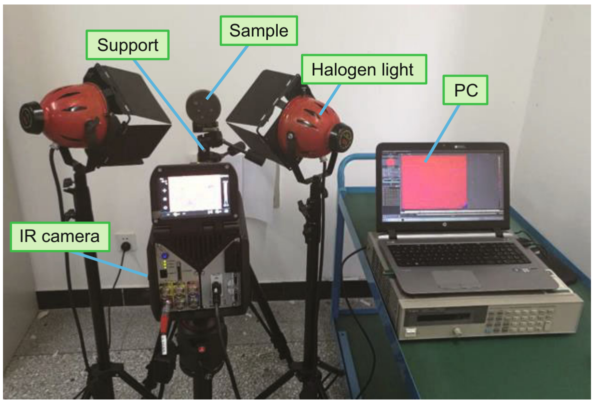

Fig. 9 Experimental setup

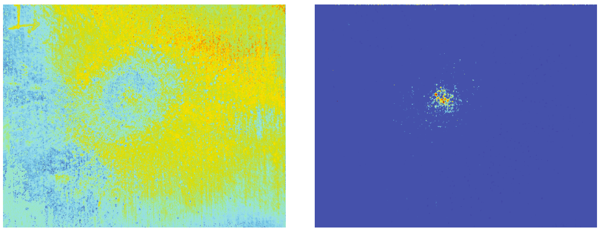
(a) (b)

Fig. 10 Results of the variational Bayesian method (material I): (a) surface; (b) subsurface

image (Fig. 10b), it can be seen that noise at the edge of the image caused by data acquisition has been eliminated, and the prominent noise caused by the independence assumption (Yang et al., 2018) of the pixels has been integrated into the connected damaged regions.

To integrate all types of damage, sparse representation was used to fuse them. A dictionary of two materials was built by the thermal image sequence; we set $K = 5$ to extract frames with different temperature distributions (Fig. 12). Specifically, Fig. 12a represents the background of material I. Different types of damage can be displayed as seen in Figs. 12b–12e. These images were then normalized and used to learn the dictionary. In the process of learning the dictionary, we set $G = 100$, $\tau = 8$, and $\varepsilon = 0.1$. The number of atoms in the dictionary was set to 1280 ($F_{\mathrm{D}} = 1280$). Finally, the dictionary of the two materials is shown in Fig. 13.

Based on the dictionary, the sparse coefficients of the surface image shown in Fig. 10a and the subsurface image shown in Fig. 11 can be derived.

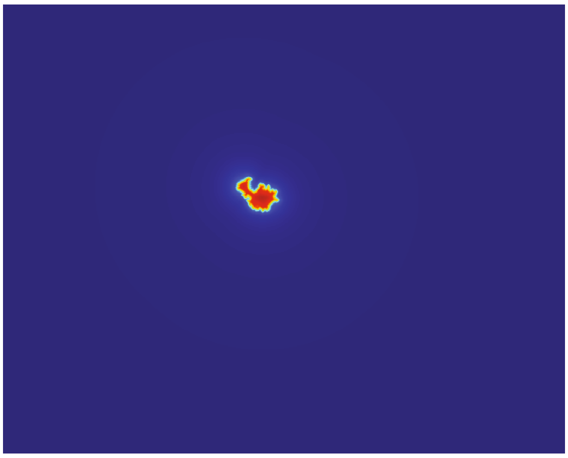

Fig. 11 Result of noise elimination (material I)

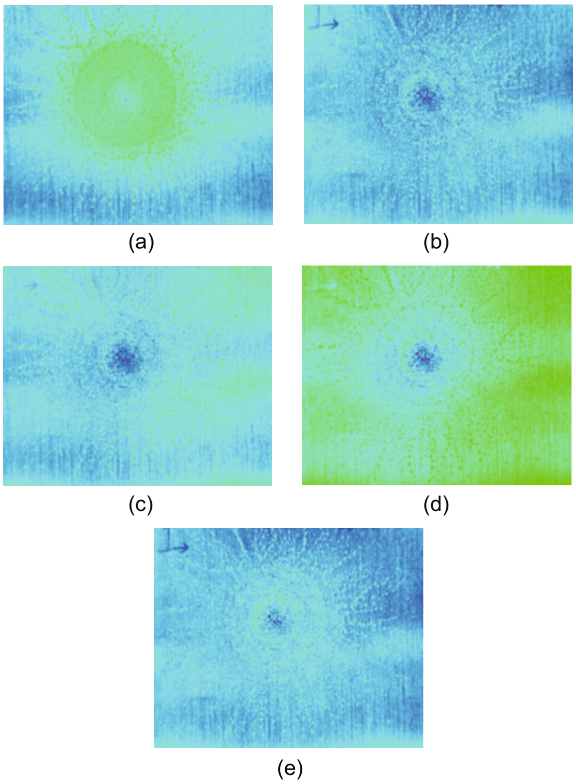

(a) (b) (c) (d) (e)

Fig. 12 Results of K-means clustering: (a) 1^{st} frame; (b) 2^{nd} frame; (c) 3^{rd} frame; (d) 4^{th} frame; (e) 5^{th} frame

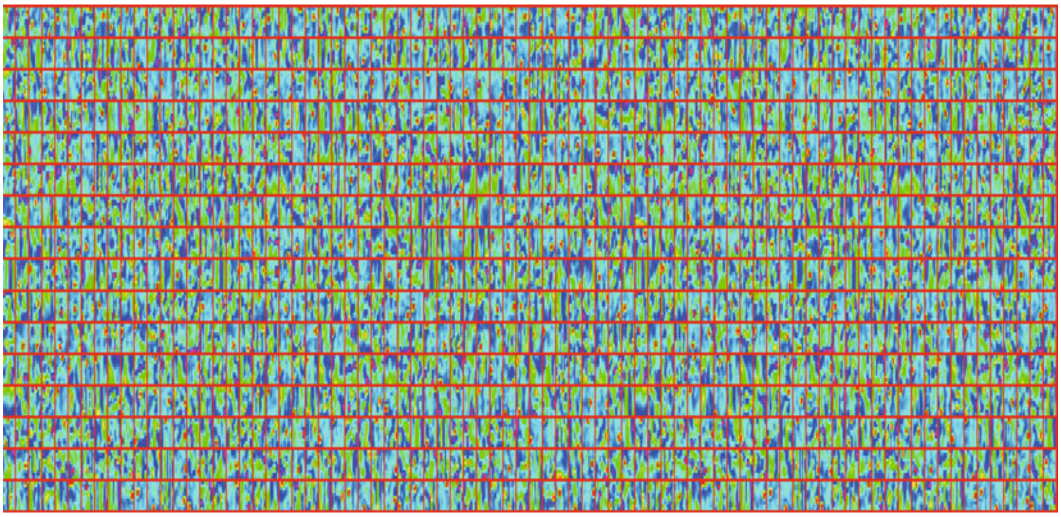

Fig. 13 Dictionary

Moreover, the two images were fused based on $\boldsymbol{H}_{\text{fusion}} = \max\{\boldsymbol{H}_{\text{F}}, \boldsymbol{H}_{\text{B}}\}$. Finally, the fused images of material I were obtained by multiplying the fused sparse coefficients with the dictionary. The results are shown in Fig. 14.

For material II, the parameters of VB remained unchanged, and the results of damage mining are displayed in Fig. 15. There were also some noise around the subsurface damage (Fig. 15b). Then, an energy function was used to eliminate noise. The number of iterations was set to 50. The value of pixel was set to $\boldsymbol{S}_{\text{B}}^{*} = \boldsymbol{S}_{\text{B}_{\max}} * H_{\varepsilon}(\vartheta^{*})$. The resulting image after noise elimination is shown in Fig. 16. Then, the dictionary (Fig. 13) was applied to compute the sparse coefficients of the surface damage image displayed in Fig. 15a and the subsurface damage image displayed in Fig. 16, and $\boldsymbol{H}_{\text{fusion}} = \max\{\boldsymbol{H}_{\text{F}}, \boldsymbol{H}_{\text{B}}\}$ was used to fuse these sparse coefficients. The resulting fused image is shown in Fig. 17.

Finally, Figs. 14–17 show the fused images of materials I and II, in which the positions of subsurface damage are highlighted in the red circle. These fused images were more blurred in comparison with their original images, since the sparse representation represents the original image with fewer features. To save computing resources in the actual calculation, one can first derive the downsampling images and then obtain the sparse coefficients. Moreover, the distribution of the impact kinetic energy of the secondary debris cloud can be identified by analyzing the fused image. The presence of subsurface damage also means higher impact kinetic energy. By checking the locations and sizes of the different types of damage in the fused image, an effective assessment of the hypervelocity impact damage can be achieved.

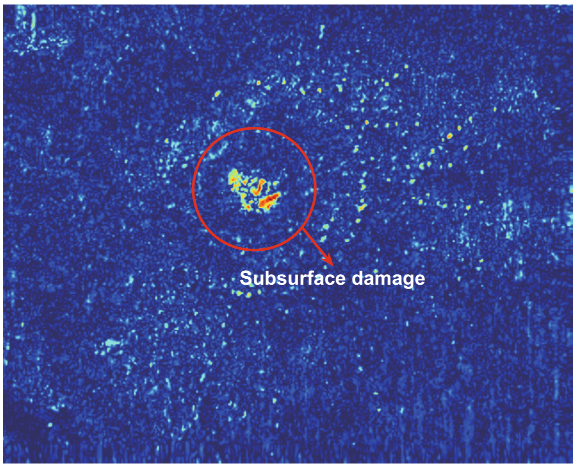

Fig. 14 Fused image (material I)

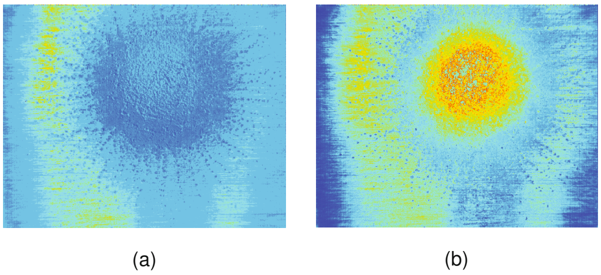

Fig. 15 Results of the variational Bayesian method (material II): (a) surface; (b) subsurface

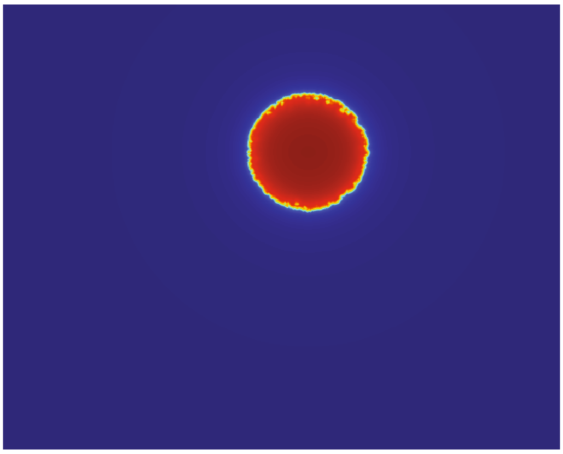

Fig. 16 Result of noise elimination (material II)

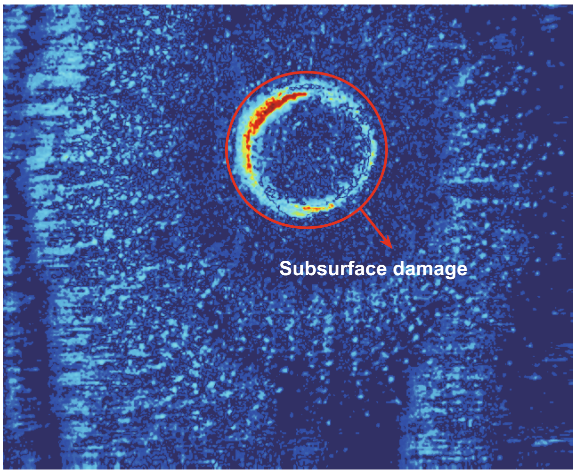

Fig. 17 Fused image (material II)

4 Conclusions

To achieve the assessment of the complex damage caused by hypervelocity impact of space debris, a multi-area damage-mining model has been proposed to extract the different types of damage in IR image sequences. To further visualize the damages using images, the VB method has been applied to estimate these parameters of the model. Since the independence assumption of the pixels is contrary to the actual situation, an energy function has been proposed to comprehensively consider the temperature distribution of the pixels in the damaged areas. In the experiment, two test samples of a rear wall with hypervelocity impact damages caused by debris cloud were evaluated by the above-mentioned method. The damage-related images were solved by VB. The locations of the different types of damage can be compared using an image-processing framework. Finally, the damage assessment of hypervelocity impact can be completed.

Contributors

Xuegang HUANG designed the research. Xuegang HUANG and Anhua SHI processed the infrared thermal image sequence data. Jinyang LUO and Qing LUO designed the hypervelocity impact experiment. Xuegang HUANG drafted the paper. Anhua SHI helped organize the paper. Xuegang HUANG revised and finalized the paper.

Compliance with ethics guidelines

Xuegang HUANG, Anhua SHI, Qing LUO, and Jinyang LUO declare that they have no conflict of interest.

References

Chen SY, Cheng ZY, Liu C, 2019. A blind stopping condition for orthogonal matching pursuit with applications to compressive sensing radar. *Signal Process*, 165:331-342. https://doi.org/10.1016/J.SIGPRO.2019.07.022

Gao B, Woo WL, Tian GY, et al., 2016a. Electromagnetic thermography nondestructive evaluation: physics-based modeling and pattern mining. *Sci Rep*, 6:25480. https://doi.org/10.1038/srep25480

Gao B, Woo WL, He YZ, et al., 2016b. Unsupervised sparse pattern diagnostic of defects with inductive thermography imaging system. *IEEE Trans Ind Inform*, 12(1):371-383. https://doi.org/10.1109/TII.2015.2492925

Geng XR, Ji LY, Sun K, 2016. Non-negative matrix factorization based unmixing for principal component transformed hyperspectral data. *Front Inform Technol Electron Eng*, 17(5):403-412. https://doi.org/10.1631/FITEE.1600028

Guo ZB, Zhang Y, 2019. A sparse corruption non-negative matrix factorization method and application in face image processing & recognition. *Measurement*, 136:429-437. https://doi.org/10.1016/j.measurement.2018.12.087

Huang XG, Yin C, Ru HQ, et al., 2020. Hypervelocity impact damage behavior of B_4C/Al composite for MMOD shielding application. *Mater Des*, 186:108323. https://doi.org/10.1016/J.MATDES.2019.108323

Kang B, Zhu WP, Liang D, et al., 2019. Robust visual tracking via nonlocal regularized multi-view sparse representation. *Patt Recogn*, 88:75-89. https://doi.org/10.1016/j.patcog.2018.11.005

Kokkinos Y, Margaritis KG, 2018. Managing the computational cost of model selection and cross-validation in extreme learning machines via Cholesky, SVD, QR and eigen decompositions. *Neurocomputing*, 295:29-45. https://doi.org/10.1016/J.NEUCOM.2018.01.005

Kullback S, Leibler RA, 1951. On information and sufficiency. *Ann Math Stat*, 22(1):79-86. https://doi.org/10.1214/AOMS/1177729694

Li X, Sun J, Xiao F, 2016. An efficient prediction framework for multi-parametric yield analysis under parameter variations. *Front Inform Technol Electron Eng*, 17(12):1344-1359. https://doi.org/10.1631/FITEE.1601225

Liou JC, Johnson NL, 2006. Risks in space from orbiting debris. *Science*, 311(5759):340-341. https://doi.org/10.1126/science.1121337

Ma XL, Hu SH, Liu SQ, et al., 2018. Multi-focus image fusion based on joint sparse representation and optimum theory. *Signal Process Image Commun*, 78:125-134. https://doi.org/10.1016/J.IMAGE.2019.06.002

Peng YG, Ganesh A, Wright J, et al., 2012. RASL: robust alignment by sparse and low-rank decomposition for linearly correlated images. *IEEE Trans Patt Anal Mach Intell*, 34(11):2233-2246. https://doi.org/10.1109/TPAMI.2011.282

Sasmaz E, Mingle K, Lauterbach J, 2015. High-throughput screening using Fourier-transform infrared imaging. *Engineering*, 1(2):234-242. https://doi.org/10.15302/J-ENG-2015040

Sun J, Chen QD, Sun JN, 2019. Graph-structured multitask sparsity model for visual tracking. *Inform Sci*, 486:133-147. https://doi.org/10.1016/j.ins.2019.02.043

Wang ZY, Zhu R, Fukui K, 2018. Cone-based joint sparse modelling for hyperspectral image classification. *Signal Process*, 144:417-429. https://doi.org/10.1016/j.sigpro.2017.11.001

Wu T, Shi J, Jiang XM, et al., 2018. A multi-objective memetic algorithm for low rank and sparse matrix decomposition. *Inform Sci*, 468:172-192. https://doi.org/10.1016/j.ins.2018.08.037

Yang Y, Cong XC, Long KY, et al., 2018. MRF model-based joint interrupted SAR imaging and coherent change detection via variational Bayesian inference. *Signal Process*, 151:144-154. https://doi.org/10.1016/j.sigpro.2018.05.007

Yin C, Xue T, Huang XG, et al., 2019. Research on damages evaluation method with multi-objective feature extraction optimization scheme for M/OD impact risk assessment. *IEEE Access*, 7:98530-98545. https://doi.org/10.1109/ACCESS.2019.2930114

Zhang HN, Huang XG, Yin C, et al., 2020. Design of hypervelocity-impact damage evaluation technique based on Bayesian classifier of transient temperature attributes. *IEEE Access*, 8:18703-18715. https://doi.org/10.1109/ACCESS.2020.2968398

Zong JJ, Qiu TS, Li WS, 2019. Automatic ultrasound image segmentation based on local entropy and active contour model. *Comput Math Appl*, 78(3):929-943. https://doi.org/10.1016/J.CAMWA.2019.03.022